Nano Research 2017, 10(2): 690–703
DOI 10.1007/s12274-016-1328-y
Research Article
ISSN 1998-0124
CN 11-5974/O4

Hyaluronidase-triggered anticancer drug and siRNA delivery from cascaded targeting nanoparticles for drug-resistant breast cancer therapy

Jie Ding[1,2], Tingxizi Liang[1], Ying Zhou[1], Zhiwei He[2], Qianhao Min[1] (✉), Liping Jiang[1] (✉), and Junjie Zhu[1] (✉)

[1] *State Key Laboratory of Analytical Chemistry for Life Science, School of Chemistry and Chemical Engineering, Nanjing University, Nanjing 210093, China*

[2] *Guangdong Provincial Key Laboratory of Medical Molecular Diagnostics, China-America Cancer Research Institute, Guangdong Medical University, Dongguan 523808, China*

Received: 22 July 2016
Revised: 7 October 2016
Accepted: 12 October 2016

KEYWORDS
drug-resistant breast cancer,
siRNA,
breast tumor cell-penetrating peptide,
hyaluronic acid,
rattle mesoporous silica

ABSTRACT

Drug resistance renders standard chemotherapy ineffective in the treatment of connective tissue growth factor (CTGF)-overexpressing breast cancer. By co-embedding the breast tumor cell-penetrating peptide (PEGA-pVEC) and hyaluronic acid (HA) as a targeting media, novel cascaded targeting nanoparticles (HACT NPs) were created on a rattle mesoporous silica (rmSiO_2) scaffold for the pinpoint delivery of siRNAs along with an anticancer drug, aiming at overcoming the drug resistance of CTGF-overexpressing breast cancer *in vivo*. The targeting nanoparticles selectively accumulated in the vasculature under the guidance of the PEGA-pVEC peptide, cascaded by receptor-mediated endocytosis with the aid of another targeting agent, HA, presenting a greater *in vivo* tumor targeting ability than single targeting ligand vectors. In addition, an HA shell prevented the leakage of therapeutic drugs during the cargo transport process, until the hyaluronidase (HAase)-triggered degradation upon lysosomes entering, guaranteeing a controllable drug release inside the target cells. When the protective shell disintegrates, the released siRNA took charge to silence the gene associated with drug resistance, CTGF, thus facilitating doxorubicin-induced apoptosis. The cascaded targeting media (PEGA-pVEC and HA) advances precision-guided therapy *in vivo*, while the encapsulation of siRNAs into a chemotherapy drug delivery system provides an efficient strategy for the treatment of drug resistance cancers.

1 Introduction

Breast cancer is the most common type of cancer among women worldwide, and the 5-year survival rate within the localized disease is 98.6%; however, the survival rate falls below 25% if cancer cells invade

Address correspondence to Junjie Zhu, jjzhu@nju.edu.cn; Qianhao Min, minqianhao@nju.edu.cn; Liping Jiang, jianglp@nju.edu.cn

and disseminate to distant sites [1, 2]. Resistance to regular chemotherapy poses a typical disadvantage in tumor treatment that always exerted a negative influence on the cure rate of breast cancer. As a member of the CCN protein family (named for its original members cry61, CTGF, and NOV), connective tissue growth factor (CTGF) can bind to integrins on the breast cancer cell surface and collaborate with matrix metalloproteinases [3–5]. CTGF overexpression has been linked to tumor size increase, lymph node metastasis, and, particularly, the resistance to cancer drug-induced apoptosis, thus causing a poor response to chemotherapy [6–8]. On the genetic level, CTGF overexpression induces the dramatic upregulation of Bcl-xL and the cellular inhibitor of apoptosis protein 1 (cIAP1), which is the true cause of the resistance to chemotherapeutic agents inducing apoptosis [9]. A knockdown of Bcl-xL or cIAP1 with small interfering RNA (siRNA), RNA interference (RNAi) could be an effective avenue to downregulate CTGF expression and abolish the CTGF-mediated resistance to drug-induced cell apoptosis. However, the inherent drawbacks of siRNAs, such as degradation by enzymes and rapid elimination by the metabolic system, limit the efficiency of direct delivery of therapeutic siRNA into the cytoplasm of the target cells [10–12]. Thus, the development of a highly effective and pinpoint siRNA-involved drug delivery system becomes a prerequisite for implementing the function of siRNAs in circumventing drug resistance.

Nanomedicine applies the principles and methods of nanoscience and nanotechnology into medicine, in which a number of nanostructures have been designed and modified to respond to multiple stimuli or as targeted carriers for drug delivery [13–16]. Across a wide variety of nanocarriers, mesoporous silica nanomaterials (MSNs) with a hollow and rattle structure (rattle mesoporous silica nanoparticles, rmSiO_2 NPs) show a particularly high efficiency for drug loading and flexibility for functional integration. In this architecture, the hollow space can control the loading and release of bioactive molecules while the core particle may respond to the external stimuli and trigger fluorescent or magnetic signals [17, 18]. Despite the functional merits of rmSiO_2 NPs for drug delivery, there are two barriers hindering the NPs from penetration *in vivo*—the basement membrane and microvascular endothelium—which lead to NP accumulation near the vasculature and NP uptake into the cells on the tumor periphery [19, 20].

The vasculature and connective tissue are essential channels that provide NPs with access to a solid tumor for cancer therapy and imaging [21, 22]. However, the penetration of NPs into the tumor interstitium is impeded by the abnormal transcapillary pressure gradient and interstitial fluid pressure induced by angiogenesis [23, 24]. The modification of targeting molecules on the surface of NPs may tackle these obstacles by providing a guide to achieve a controllable biodistribution and pinpointed drug release *in vivo* [25, 26]. An effective and specific vector for breast cancer therapy is a breast tumor homing, cell-penetrating peptide (PEGA-pVEC) [27]. This peptide is composed of two components: a tumor-specific vascular homing peptide (PEGA) for identifying the higher expressive marker molecule (membrane-bound proline-specific amino peptidase P, APasep) in the vasculature of breast cancer [28] and a cell-penetrating peptide (p-VEC) for transporting cargo across the cell membrane [29]. Thus, the PEGA-pVEC peptide can act as a navigator, leading NPs to accumulate in breast vasculature. On the cellular level, surface receptor-mediated endocytosis has proven to be an efficient avenue to promote drug delivery specificity. Enzymatically degradable hyaluronic acid (HA) can specifically interact with CD44, the overexpressed transmembrane glycoprotein on the surface of MDA-MB-231 breast cancer cells, and assist with cellular uptake. Meanwhile, HA is an ideal protective shell of drug vectors to enhance drug stability, avoid the damage to normal cells, and hide from the immune system assuring low premature release before drug carriers reach the diseased region [30–32]. More importantly, after endocytosis, the HA shell can be degraded by endogenous hyaluronidase (HAase) in lysosomes, allowing an oriented release of the anti-cancer drugs [33, 34]. The histological selectivity of the PEGA-pVEC peptide to the vasculature and the cellular selectivity of HA to the surface receptor, CD44, create a good opportunity for constructing an enhanced targeting bio-interface for drug delivery; intracellular degradable HA can serve as an intelligent drug coating in drug delivery systems (DDSs) for

switching on the drug release.

In this study, we prepared activatable HAase and cascaded targeting NPs ($rmSiO_2$@siRNA@Dox@HA@peptide NPs, HACT NPs) for the pinpoint delivery of anticancer drugs and siRNAs to overcome the drug resistance of CTGF-overexpressing breast cancer *in vivo*. As shown in Scheme 1(a), $rmSiO_2$ NPs were chosen as a hollow scaffold for building the drug carrier. The siRNA for the knockdown of Bcl-xL in the CTGF-overexpressing breast cancer cells was fixed on the surface of NPs while doxorubicin (Dox) was encapsulated as a conventional chemotherapeutic agent. HA was coated onto the surface of $rmSiO_2$@siRNA NPs to form a protective shell, targeting overexpressed CD44 on the surface of MDA-MB-231 breast cancer cells and performing enzyme-responsive degradation for drug release. Another targeting ligand for recognizing tumor vasculature, the PEGA-pVEC peptide, was conjugated on the HA shell with an aminoxatyl reaction. After injected into the blood vessel (Scheme 1(b)), the HACT NPs accumulated in tumor vessels by the active targeting recognition of peptide to vascular marker and selectively taken up by CD44-rich cancer cells, in which the high level of HAase in the lysosomes activated the degradation of the HA shell, thereby releasing Dox and siRNA to induce apoptosis. The presented HACT NPs had a set of advantages over conventional drug-loaded NPs: (1) the cascaded targeting ligands, PEGA-pVEC peptide and HA, allowed HACT NPs to pass through multiple barriers and get access to cancer cells, ensuring the high selectivity to breast cancer on a tissue and cellular level; (2) HAase-triggered degradation of the HA shell in lysosomes enabled the stimuli-responsive drug release in target cells, while preventing drug leakage in transportation; (3) siRNA-involved drug delivery system could silence the gene associated with drug resistance, which endowed HACT NPs with a better therapeutic effect on CTGF-overexpressing breast cancer; and (4) hollow structured $rmSiO_2$ NPs with a high loading capacity provided an excellent carrier of synergistic therapeutic drugs for breast cancer.

2 Experimental

2.1 Materials

Tetraethyl orthosilicate (TEOS), 1-ethyl-3-(3-dimethylaminopropyl) carbodiimide hydrochloride (EDC), N-hydroxysuccinimide (NHS), polyvinyl

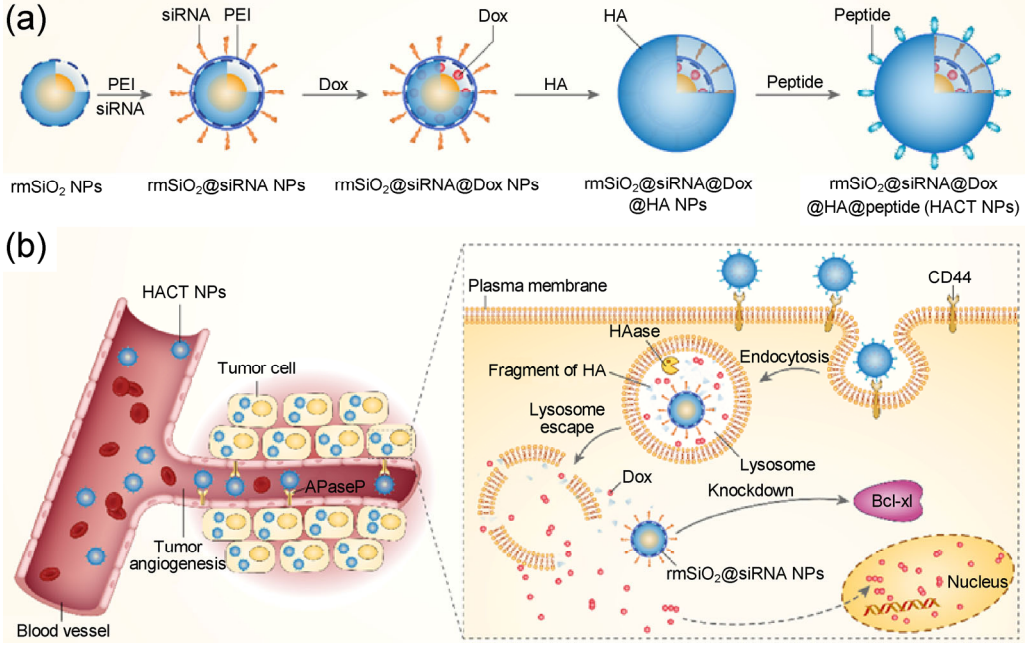

Scheme 1 (a) Schematic diagram of the "layer-by-layer assembly" strategy for the construction of HACT NPs with the cascade of two targeting agents (HA and peptide) and two cancer therapeutic agents (siRNA and Dox). (b) Schematic illustration of HACT NPs for the selective and efficient treatment of CTGF-overexpressing breast cancer.

pyrrolidone (PVP, M_W ~ 40,000 and 8,000), hyaluronidase were obtained from Sigma-Aldrich (St. Louis, MO, USA). Peptides (cCPGPEGAGC-LLIILRRRIRKQAHAHSK-NH_2) and siRNA (5′-AGGAGAGAAAGUCAACC ACCAGCUC-3′) were synthesized by Life Technologies and GenePharma, respectively. Polyetherimide (PEI, M_W ~ 10,000) and sodium hyaluronate (M_W ~ 100,000) were purchased from Aladdin. L15 medium, 1640 medium, and Dox were obtained from KeyGEN BioTECH. Cell counting kit-8 (CCK-8) kit, Annexin V-FITC, and PI were purchased from Dojindo Molecular Technologies, Inc. Fetal bovine serum (FBS) and antibodies were obtained from Gibco. Acrylamide, tris(hydroxymethyl)-aminomethane (Tris), sodium dodecyl sulfate (SDS), ammonium persulfate (APS), tetramethylethylene-diamine (TEMED), dithiothreitol (DDT), glycine (Gly), hydrochloric acid (36%), and bromophenol blue (BPB) were from Sinopharm Chemical Reagent Co., Ltd. Yili skimmed milk powder was bought from the supermarket. Ultrapure water was used in all experiments. All chemicals were used as received without further purification.

2.2 Fabrication and characterization of HACT NPs

First, $rmSiO_2$ NPs were prepared using an improved "surface-protected etching" method [17]. 2.5 mL ammonium hydroxide, 0.835 mL ultrapure water and 40 mL ethanol were mixed and preheated to 50 ℃, followed by the addition of 1.92 mL TEOS. After stirring for 6 h, the mixture was cooled to room temperature and stirred for another 2 h. The product was centrifuged, washed with water, and re-dispersed in 5 mL water. Subsequently, the product was mixed with 3 mL PVP (0.8 g in H_2O, M_W ~ 40,000) and then refluxed at 95 ℃ for 3 h to obtain SiO_2@PVP (core) NPs. After washing three times with ultrapure water and ethanol, the core NPs were collected by centrifugation. For coating the SiO_2 shell, the core NPs were dispersed in 80 mL ethanol with ultrasonic processing, followed by the sequential addition of 1.67 mL H_2O, 5 mL ammonium hydroxide solution, and 3.84 mL TEOS. The mixture was kept at room temperature for 3 h while stirring. The final product was collected by centrifugation, dispersed in 10 mL water, mixed with 3 g PVP (M_W ~ 8,000), and then refluxed for 3 h at 95 ℃. After being cooled down to room temperature and washed three times with ultrapure water, the product was mixed with a NaOH aqueous solution (5 mL, 0.20 g/mL) to initiate etching. After being etched for 3 h, $rmSiO_2$ NPs were collected by centrifugation, and washed several times with ultrapure water. The synthesis process was characterized with a JEOL JEM-200CX transmission electron microscope (TEM) and 90Plus dynamic light scattering (DLS).

To obtain $rmSiO_2$@siRNA NPs, $rmSiO_2$ NPs should first be coated with PEI (M_W ~ 10 kD). 0.2 g $rmSiO_2$ NPs were dispersed in an absolute ethanol solution containing 0.1 g PEI. After sonication and stirring for 30 min, the PEI-coated $rmSiO_2$ NPs were washed with phosphate buffered saline (PBS) and dispersed in diethy pyrocarbonate (DEPC) water. Next, siRNA (5′-AGGAGAGAAAGUCAACCACCAGCU C-3′) was added and captured by $rmSiO_2$ NPs via electrostatic attraction to acquire $rmSiO_2$@siRNA NPs. 0.1 μg siRNA was mixed with 0.4–3.5 μg PEI-$rmSiO_2$ NPs in DEPC water to obtain particle/nuclei acid (P/N) ratios of 4:35; 10 μL of the polyplex solution was mixed with 2 μL loading buffer and electrophoresed in a 1.5% agarose gel containing 0.5 μg/mL ethidium bromide at 100 V for 30 min in Tris/borate/EDTA (TBE) running buffer (pH = 8).

Dox was loaded inside $rmSiO_2$@siRNA NPs as follows: 5 mg $rmSiO_2$@siRNA NPs was incubated in the solution of Dox (1 mg/mL, 1 mL) for 24 h while stirring at room temperature, followed by centrifugation to remove any free Dox. In order to prevent drug leakage in the way of delivery and undesired release in cells, the pores on the surface of $rmSiO_2$@siRNA@Dox NPs should be sealed by HA. In detail, 1 mg HA was added to the suspension of $rmSiO_2$@siRNA@Dox NPs and stirred for another 24 h, followed by centrifugation, and repeated washing with PBS (10 mM, pH = 7.4). The loading amount of Dox was 165 μg/mg $rmSiO_2$@siRNA NPs, which was calculated from the supernatant concentration of Dox.

The NH_2-containing peptide (cCPGPEGAGC-LLIILRRRIRKQAHAHSK-NH_2) was conjugated to the carboxyl-containing $rmSiO_2$@siRNA@Dox@HA NPs via covalent amide bond involving EDC/NHS activation of carboxylic acids and the following amidation reaction. The $rmSiO_2$@siRNA@Dox@HA NPs suspension (150 μL, 10 μg/mL) was treated with 400 mM EDC and 100 mM

NHS in pH = 6.0 2-(N-morpholino)ethanesulfonic acid (MES) for 15 min at room temperature while stirring. The active NPs were washed twice using ultrapure water to remove unreacted EDC and NHS. Then, the peptide was added into the NP suspension at a mass ratio of 10% to NPs and agitated for 2 h at room temperature. The final product (HACT NPs) was washed twice using ultrapure water and resuspended in PBS (10 mM, pH = 7.4) for the next application.

2.3 Drug release experiments

To investigate the effect of HAase on Dox release at different pH values, the rmSiO$_2$@siRNA@Dox and rmSiO$_2$@siRNA@Dox@HA NPs were dispersed in the 20 mL aqueous buffer solutions (10 mM PBS, pH = 7.4; 10 mM acetate buffer, pH = 5.0) with or without HAase (150 U/mL) at room temperature. Aliquots (0.5 mL) were taken from the suspension at pre-determined time intervals and replaced with an equal volume of fresh medium. The concentration of released Dox was determined by measuring with a UV–Vis spectra at 480 nm based on the standard curve.

2.4 Cell culture and cell cytotoxicity assay

The CTGF-overexpressing breast cancer cell line (MDA-MB-231) and control breast cancer cell line (MCF-7) were cultured following protocols provided by the American type Tissue Culture Collection (ATCC). Both breast cancer cells have different culture conditions. MDA-MB-231 cells were cultured in L15 medium containing FBS (10%, v/v), penicillin (100 U/mL), and streptomycin (100 μg/mL) in an incubator (ThermoFlash Scientific) at 37 ℃ under atmospheric conditions and 90% relative humidity. The cells were sub-cultivated approximately every 3 days at 80% confluence using trypsin (0.25%, w/v) at a split ratio of 1:5. The culture conditions of MCF-7 cells were changed to Dulbecco's modified Eagle medium (DMEM) and an atmosphere with 5% CO_2. MDA-MB-231 and MCF-7 cells (1×10^4 cells/well) were seeded in 96-well plates and cultured for 24 h. The cells were exposed to Dox, rmSiO$_2$@Dox NPs, rmSiO$_2$@Dox@HA NPs, rmSiO$_2$@siRNA@Dox NPs, and rmSiO$_2$@siRNA@ Dox@HA NPs at different concentrations of Dox for 24 h. CCK-8 solution (10 μL) was added into each well and cultured for 2 h. The absorbance (abs.) was measured at 450 nm with a full wavelength scanning multi-function reader (Varioskan Flash, ThermoFisher Scientific). The cell inhibition ratio was determined using the following equation

Cell inhibition ratio (%) = 1 – (mean abs. value of treatment group/mean abs. value of control) × 100%

The half-maximal inhibition concentration (IC_{50}) was calculated according to Huber and Koella [35].

2.5 Site-specific delivery

MDA-MB-231 cells (1×10^5 cells/dish) were seeded in a confocal microscopy dish and cultured for 24 h. For the site-specific delivery assay, the cells were stained with LysoTracker Green (1 μL, Invitrogen) at 37 ℃ for 15 min. Afterwards, the cells were washed with ice cold PBS twice, and incubated with Dox, rmSiO$_2$@BHQ2@Dox NPs, or rmSiO$_2$@BHQ2@Dox@HA NPs in complete medium at 37 ℃ for 1, 2, and 4 h. The cells were washed with ice cold PBS twice and immediately observed using confocal laser scanning microscope (CLSM) (TCS SP5, Leica).

2.6 *In vitro* cytotoxicity

To study the cell apoptosis induced by Dox, rmSiO$_2$@Dox NPs, rmSiO$_2$@Dox@HA NPs, rmSiO$_2$@siRNA@Dox NPs, and rmSiO$_2$@siRNA@Dox@HA NPs on MDA-MB-231 cells at 30 μg/mL of Dox, a flow cytometry assay and confocal imaging assay of Annexin V-FITC and PI was employed. Cells were cultured for 24 h and then harvested, stained, and determined using flow cytometry (FC500, BECKMAN) or CLSM (TCS SP5, Leica). The flow cytometry data were analyzed with FCS Express V3.

2.7 Western blot analysis

An immunoblotting analysis was performed as previously described [9]. Briefly, MDA-MB-231 cells were seeded into 6 cm dishes (1×10^6 cells/dish) and allowed to adhere overnight. The cells were then incubated with rmSiO$_2$ NPs, Dox, rmSiO$_2$@Dox NPs, rmSiO$_2$@Dox@HA NPs, rmSiO$_2$@siRNA@Dox NPs, or rmSiO$_2$@siRNA@Dox@HA NPs with 30 μg/mL of Dox for 24 h. Afterwards, detergent-solubilized whole-cell extracts (WCE) were prepared by lysing the cells. The clarified WCE (20 mg/lane) were separated using a 10% sodium dodecyl sulfate-polyacrylamide gel electro-

phoresis (SDS-PAGE), transferred electrophoretically to nitrocellulose membranes, and immunoblotted with primary antibodies, such as anti-p-ERK, anti-PARP, anti-clAP1, anti-CTGF, anti-p-FAK, anti-Bcl-xL, or anti-β-actin.

2.8 Tumor growth and *in vivo* therapeutic treatment

All animal studies were performed in accordance with the Institutional Animal Care and Use Committee. MDA-MB-231 cells (1×10^6) were engrafted into the right forelimb of 4-week-old female nude mice. When the tumor volumes reached 50 mm^3, the animals were treated with each sample. Tumor-bearing mice were injected with saline water, $rmSiO_2$ NPs, Dox, $rmSiO_2$@Dox@HA NPs, $rmSiO_2$@siRNA@Dox@HA NPs, or HACT NPs with 3 mg/kg Dox. Each formulation was injected six times at three-day intervals. Tumor volumes were measured and the mice were weighed every two days. The relative tumor volumes were calculated for each mouse as V/V_0 (V_0 was the tumor volume when the treatment was initiated). The tumor inhibition ratio was determined using the following equation

Tumor inhibition ratio (%) = 1 − (mean weight of treatment group/mean weight of control) × 100%

2.9 Histological analysis

The samples were stained with hematoxylin and ethanol (H&E) to evaluate the presence of tissue injuries. Briefly, the samples (tumor, heart, liver, spleen, lung, kidney, brain, and small intestine) were fixed with 10% formalin, rehydrated with 70% ethanol, and rinsed with deionized water before hematoxylin staining. Samples were then rinsed with water, decolorized with acid alcohol, immersed in lithium carbonate, and rinsed again with water. Next, the eosin counterstain was applied and slides were dehydrated with 100% ethanol, rinsed with xylene, and mounted on a coverslip with Biomount. The images were obtained using a Nikon Eclipse 90i microscope.

3 Results and discussion

3.1 Layer-by-layer assembly of HACT NPs

The HACT NPs were fabricated via a layer-by-layer assembly method to encapsulate Dox and siRNA in the different locations of $rmSiO_2$ NPs. An HA layer coated the surface of $rmSiO_2$ NPs, followed by further modification of the peptides. First, $rmSiO_2$ NPs were prepared using an improved "surface-protected etching" method. TEM images and particle size distributions were used to record the gradually forming process (Fig. 1(a) and Fig. S1 in the Electronic Supplementary Material (ESM)). After the SiO_2 core (40 nm) was obtained, double layers of PVP at different molecular weights (inner M_W ~ 40,000 and outer M_W ~ 8,000) with an interlayer of dense silica were coated on it in a stepwise manner. By partially etching the silica layer in sodium hydroxide solution, a sandwich hollow space with a thickness of ~15 nm was created between the silica core and loose outer shell, and the prepared $rmSiO_2$ NPs were featured with uniform morphology and excellent dispersity. A nitrogen adsorption–desorption experiment was performed to obtain the surface area and pore information of $rmSiO_2$ NPs. In Fig. S2 (in the ESM), the nitrogen adsorption–desorption curve and pore size distribution represents 11 nm mesopores and 62 and 98 nm macropores, which were, respectively, corresponding to the pores etched in the outer shell and those formed by particle stacking.

The Brunauer–Emmett–Teller (BET) surface area and cumulative pore volume were 141.9 m^2/g and 0.726 cm^3/g, respectively, which were consistent with values in literature and conducive to drug loading [17]. For introducing siRNA, PEI (M_W ~ 10 kD) was electrostatically assembled onto the $rmSiO_2$ NPs to produce a positively charged surface, which was reflected by the zeta potential alteration from –4.96 to +8.08 mV (Fig. 1(b)). A Dox adsorption experiment showed that the coated PEI extended little influence on the permeability of the mesopores and the drug loading capacity of $rmSiO_2$ NPs (Fig. S3 in the ESM). For siRNA loading, the residual siRNA monitored by agarose gel electrophoresis (Fig. 1(c)) implied that siRNA was fully immobilized onto the $rmSiO_2$@PEI NPs at the NPs to the siRNA quality (N/P) ratio of 20:1. The slight decrease in positive surface charge shown in Fig. 1(b) further validated the siRNA immobilization. Dox was encapsulated into the cavity of $rmSiO_2$ NPs by directly mixing it with $rmSiO_2$@siRNA NPs. After

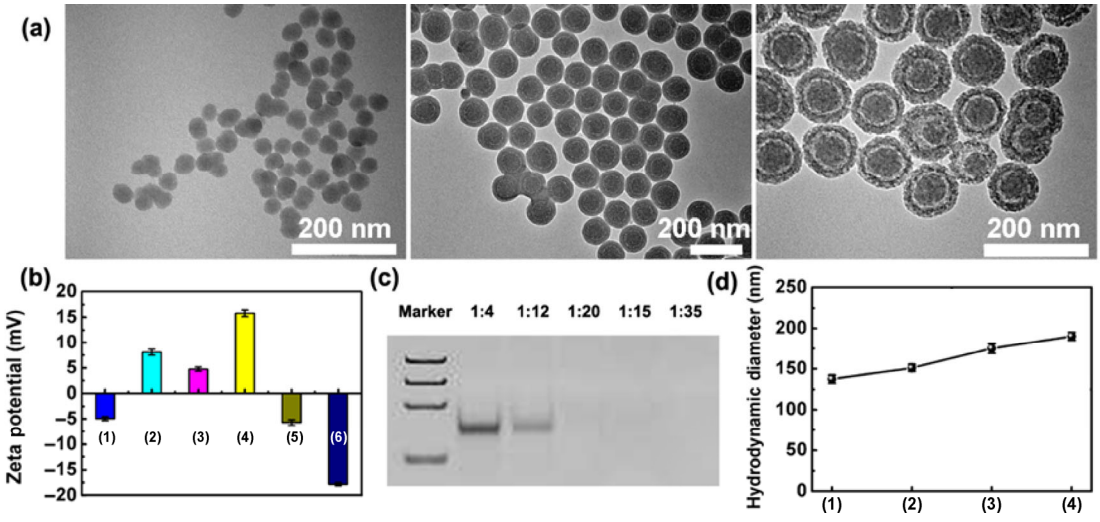

Figure 1 Characterization of the HACT NPs. (a) TEM images of SiO_2 core NPs, SiO_2@PVP(M_W ~ 40,000)@SiO_2 @PVP(M_W ~ 8,000) NPs, and rmSiO_2 NPs. (b) The zeta potential of (1) rmSiO_2 NPs; (2) rmSiO_2 NPs@PEI NPs; (3) rmSiO_2@siRNA NPs; (4) rmSiO_2@siRNA@Dox NPs; (5) rmSiO_2@siRNA@Dox@HA NPs; and (6) HACT NPs. (c) Agarose gel electrophoresis of rmSiO_2@PEI NPs to which siRNA was complexed at various NPs to nucleic acid ratios. (d) The hydrodynamic diameter of (1) rmSiO_2 NPs; (2) rmSiO_2@siRNA NPs; (3) rmSiO_2@siRNA@HA NPs; and (4) HACT NPs.

drug loading, HA was used for capping the NPs to prevent undesired release and promote the target ability, leading to a distinct surface charge inversion. After coating the outermost peptide layer, the zeta potential saw a dramatic decline from –5.7 to –17.8 mV, demonstrating the assembly of electronegative peptides. Moreover, DLS was performed to monitor the layer-by-layer assembly process (Fig. 1(d)). The average hydrodynamic diameter gradually increased from 137 to 190 nm along with the systematic modification of siRNA, HA, and peptides, confirming the multi-layered structure of the final nanocarriers, HACT NPs.

3.2 Enzyme triggered dox release

HA can recognize and bind to CD44 on the cellular surface to induce endocytosis. The degradation of the HA shell by HAase facilitated the release of Dox from rmSiO_2@HA NPs in lysosomes. To explore the HAase-mediated release of Dox, we first investigated the *in vitro* release profile of Dox from rmSiO_2@HA NPs in the presence and absence of the HA shell and HAase. As shown in Fig. 2(a), 36% and 26% of Dox were released within 1 h in the absence of the HA shell in pH 5.0 and 7.4 buffer solution, respectively. In contrast, the presence of the HA shell prevented the release of Dox from rmSiO_2@HA NPs, and only 1.2% and 0.5% of Dox was leaked into the buffer solution over 1 h. However, since HAase degraded the HA shell, the Dox release ratios increased to 25% and 15.6% at the same time interval. In summary, we may deduce that the efficient release of Dox, accompanied by the rapid disassociation of the HA shell could be triggered by both HAase and the acidic environment inside the lysosome of cancer cells. In this drug release system, while the rmSiO_2@HA NPs were unprotected by the degradation of HA, protons in acidic medium detached Dox from the negatively charged silica surface [31], giving a synergistic efficacy in drug release.

Before further experimentation, the biological stability of NPs needed to be examined. The average hydrodynamic diameter of HACT NPs was 190 nm in PBS and 223 nm in culture medium, which did not change for at least 120 h (Fig. 2(b)) demonstrating the long-term stability of NPs under physiological conditions. The enlarged hydrodynamic diameter in complete medium, in comparison with PBS, could be attributed to the adsorption of proteins in serum. To verify the degradation of the HA shell by HAase, we investigated the changes in hydrodynamic size and zeta potential of rmSiO_2@Dox@HA NPs in PBS and culture medium. As shown in Fig. S4 (in the ESM), the values of the hydrodynamic size and zeta potential

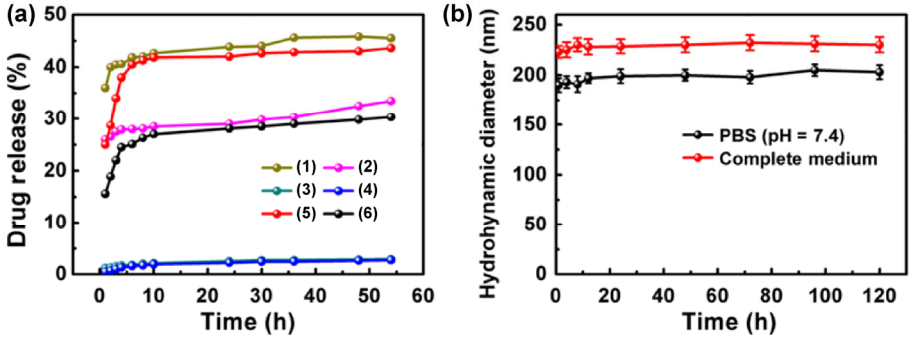

Figure 2 (a) *In vitro* release of Dox from rmSiO$_2$@Dox and rmSiO$_2$@Dox@HA NPs with or without HAase in pH 7.4 PBS and pH 5.0 acetate buffer. (1) rmSiO$_2$@Dox NPs, without HAase, pH 5.0 acetate buffer; (2) rmSiO$_2$@Dox NPs, without HAase, pH 7.4 PBS; (3) rmSiO$_2$@Dox@HA NPs, without HAase, pH 5.0 acetate buffer; (4) rmSiO$_2$@Dox@HA NPs, without HAase, pH 7.4 PBS; (5) rmSiO$_2$@Dox@HA NPs, HAase, pH 5.0 acetate buffer; and (6) rmSiO$_2$@Dox@HA NPs, HAase, pH 7.4 PBS. (b) Change in the particle size of HACT NPs after incubation at pH 7.4 PBS and complete medium over time.

reached a plateau at 6 h, exhibiting a similar trend with drug release curves.

To verify the targeted drug release function of HA-capped nanocarriers, the CTGF-overexpressing breast cancer cells (MDA-MB-231), with a high abundance of CD44 [36], were incubated with Dox, rmSiO$_2$@BHQ2@Dox NPs, or rmSiO$_2$@BHQ2@Dox@HA NPs for 1, 2, and 4 h, followed by imaging the intracellular Dox distribution using a confocal fluorescence microscope (Fig. S5 in the ESM). As a quencher, BHQ2 added to the core of rmSiO$_2$ could effectively quench the fluorescence of Dox, which was beneficial to monitor the release of Dox from NPs. Although rmSiO$_2$ NPs facilitated cellular uptake upon the electron paramagnetic resonance, compared with free Dox, the release rate of Dox from NPs relatively slowed down (Figs. S5(a) and S5(b) in the ESM). In contrast, rmSiO$_2$@HA NPs showed a significantly enhanced cell uptake and release of Dox compared to that without an HA shell (Fig. S5(c) in the ESM), in which CD44-mediated endocytosis made a major contribution to the uptake of NPs. For the cells incubated with rmSiO$_2$@BHQ2@Dox@HA NPs for 2 h, red fluorescence, ascribed to Dox, was co-localized well with LysoTracker Green, indicating that NPs were trapped in the lysosome and Dox release had been initiated. After an additional 2 h of incubation, an obvious dissociation in the signals of Dox and LysoTracker was observed, confirming the lysosomal escape of Dox and NPs. Therefore, it was rational to conclude that the HA shell was able to promote the efficiency of uptake by CD44-overexpressing cells and the HAase, in an acidic subcellular organelle, triggered the degradation of coated HA, resulting in the sentinel release of Dox from NPs.

3.3 Overcoming the drug resistance of CTGF-overexpressing breast cancer cells by siRNA-involved NPs

The *in vitro* cytotoxicity of Dox and NPs@Dox against MDA-MB-231 and MCF-7 cells (control cells) was estimated using a CCK-8 assay. To exclude the possible influence of rmSiO$_2$ NPs on cell viability, various concentrations of free NPs were incubated with MDA-MB-231 cells for 24 h and then the cell inhibition ratios were calculated. Within the test concentration range, up to 500 μg/mL, rmSiO$_2$ NPs had no obvious adverse effect on cell viability (Fig. S6 in the ESM). The drug sensitivity of MCF-7 and MDA-MB-231 cells was assessed by acquiring the inhibition ratio while increasing the drug dose. Owing to the drug resistance of MDA-MB-231 cells, the inhibition ratio of cells was about 59% with 50 μg/mL Dox after 24 h (Fig. 3(a)). In contrast, drug-sensitive MCF-7 cells were completely inhibited with 20 μg/mL Dox (Fig. 3(b)). The IC$_{50}$ of Dox was approximately 36.4 μg/mL for MDA-MB-231 cells and 3.93 μg/mL for MCF-7 cells. As expected, after treatment with rmSiO$_2$ NPs or rmSiO$_2$@HA NPs loaded with siRNA and Dox, the MDA-MB-231 cells showed significantly enhanced cytotoxicity (Fig. 3(c)). The inhibition ratio of MDA-MB-231 cells reached 80%

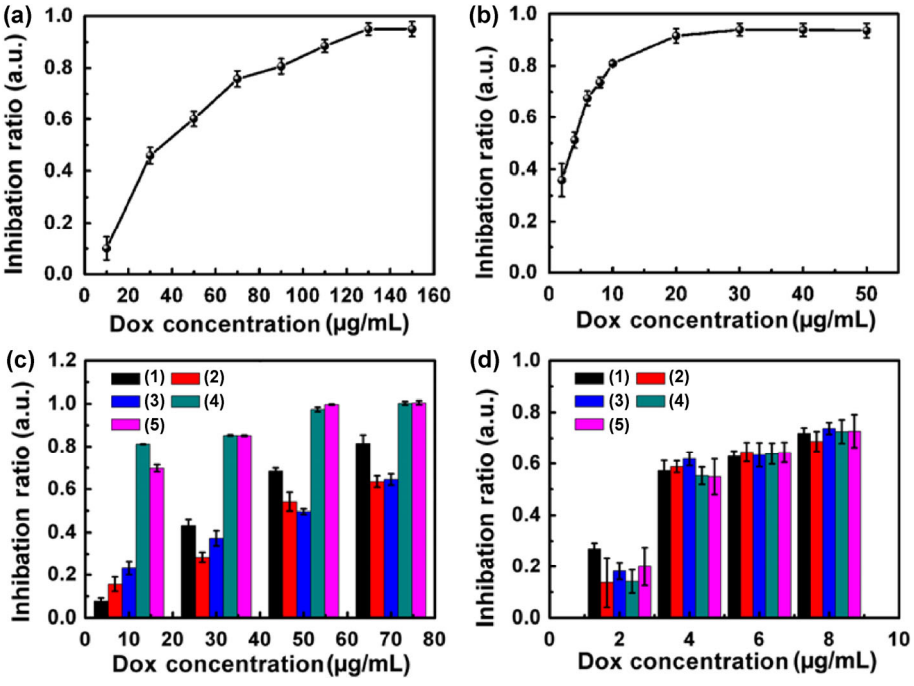

Figure 3 The *in vitro* cytotoxicity was estimated with a CCK-8 assay. MDA-MB-231 cells (a) and MCF-7 cells (b) were incubated with different concentrations of Dox for 24 h. MDA-MB-231 cells (c) and MCF-7 cells (d) were incubated with different formulations for 24 h. (1) Dox; (2) rmSiO$_2$@Dox NPs; (3) rmSiO$_2$@Dox@HA NPs; (4) rmSiO$_2$@siRNA@Dox NPs; and (5) rmSiO$_2$@siRNA@Dox@HA NPs.

after treatment with rmSiO$_2$@siRNA@Dox NPs and rmSiO$_2$@siRNA@Dox@HA NPs with 10 μg/mL Dox after 24 h, much higher than that of other formulations. Nevertheless, the same treatments had no influence on MCF-7 cells (Fig. 3(d)). The increased cytotoxicity was contributed to the knockdown of Bcl-xL with siRNA to abolish the CTGF-mediated resistance to apoptosis induced by Dox in MDA-MB-231 cells.

Next, we estimated the apoptosis-inducing effect of rmSiO$_2$ NPs and rmSiO$_2$@HA NPs loaded with siRNA and Dox using Annexin V-FITC/PI apoptosis detection. After MDA-MB-231 cells were incubated with different formulations with 30 μg/mL Dox for 24 h, the cells were stained with Annexin V-FITC/PI. As shown in Fig. 4(a), the cells treated by rmSiO$_2$@HA NPs loaded with siRNA and Dox underwent particularly significant morphological changes compared to other treatments. In the flow cytometry analysis (Fig. 4(b)), this group displayed intense fluorescence with apoptotic characteristics. The late apoptotic ratio located in the first quadrant was 87.1%, much higher than that of other formulations. The inhibition ratio, variation of cellular morphology, and stage of apoptosis caused by different drug delivery systems all indicated that rmSiO$_2$@siRNA@Dox@HA NPs, with a high gene-silencing efficiency and good targeting ability, exhibited superior apoptosis-inducing capabilities.

3.4 Sustained silencing of CTGF induced by siRNA-involved NPs

CTGF overexpression has been linked to the drug resistance, size increase, and lymph node metastasis of breast cancer, resulting in resistance to Dox-induced apoptosis by upregulation of Bcl-xL and cIAP1. The siRNA targeting Bcl-xL could effectively downregulate expression of the target proteins, addressing the drug resistance caused by CTGF overexpression. To investigate the siRNA-mediated gene-silencing efficiency of rmSiO$_2$@siRNA@Dox@HA NPs, we examined the expression of Bcl-xL, cIAP1, and CTGF using a western blot (WB) analysis. In Fig. 5(a), the rmSiO$_2$@Dox@HA NPs loaded with siRNA showed the highest gene silence efficiency in MDA-MB-231 cells overexpressing the CD44 receptor compared with other formulations, which should be attributed to the enhanced cellular uptake and efficient intracellular delivery of siRNA.

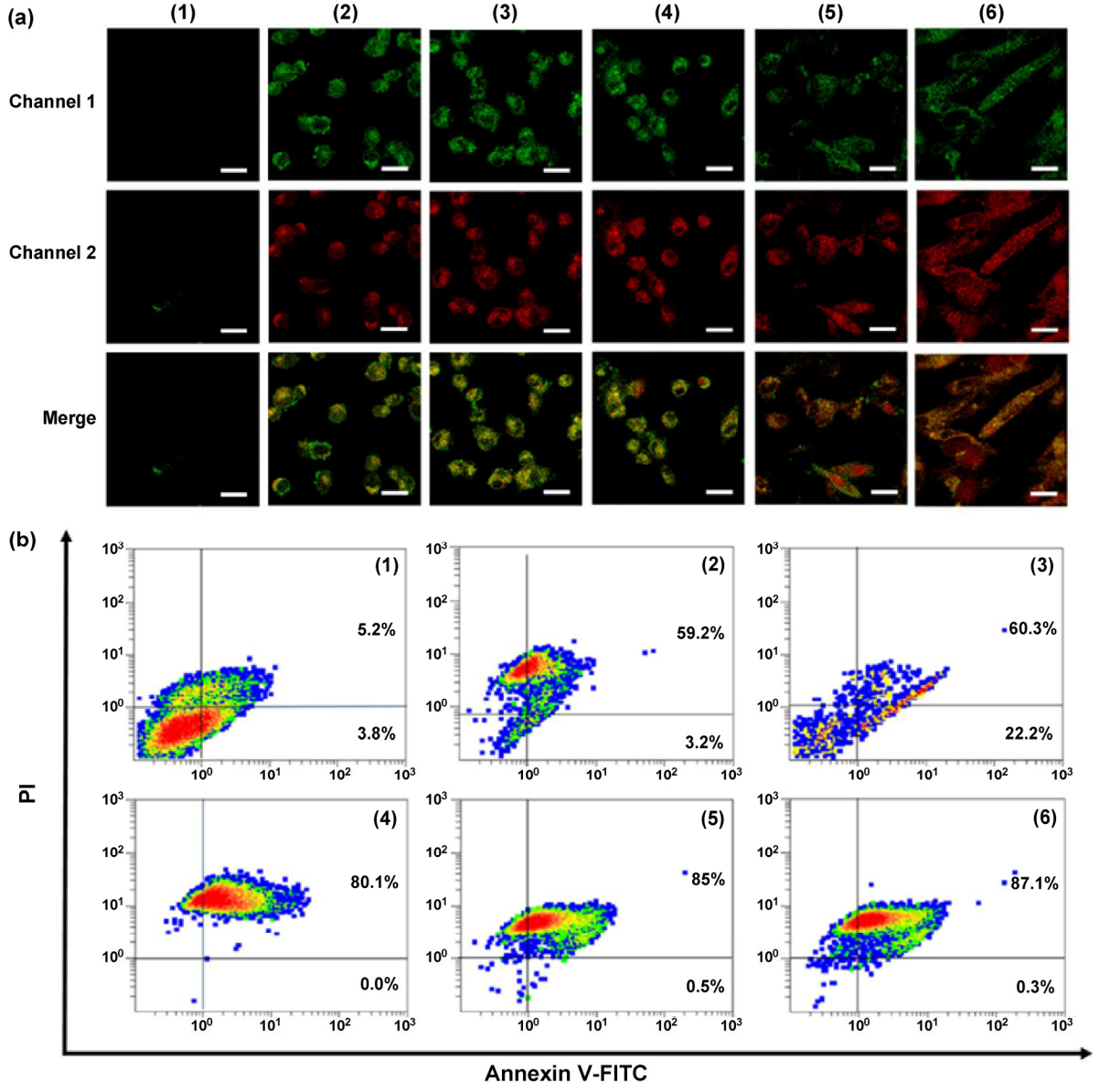

Figure 4 Confocal microscopy images (a) and the flow cytometry analysis (b) of MDA-MB-231 cell apoptosis induced by different formulations with 30 μg/mL Dox for 24 h observed using Annexin V-FITC/PI staining. (1) Control; (2) Dox; (3) rmSiO$_2$@Dox NPs; (4) rmSiO$_2$@Dox@HA NPs; (5) rmSiO$_2$@siRNA@Dox NPs; and (6) rmSiO$_2$@siRNA@Dox@HA NPs.

Therefore, it can be expected that downregulating the expression level of downstream proteins with siRNA would have a good possibility to overcome the resistance to Dox-induced apoptosis caused by the overexpression of CTGF in breast cancer cells.

CTGF exerts a range of diverse functions by binding with cell surface integrins. Most integrins activate both focal adhesion kinase (FAK) and extracellular regulated protein kinase (ERK1/2), which causes the phosphorylation of kinases. Thus, CTGF overexpression dramatically induces FAK and ERK1/2 phosphorylation. The FAK-ERK1/2 signaling pathway has previously been implicated in cellular protection from various apoptosis signals [9]. The downregulation of Bcl-xL protein expression would inhibit the activation of kinases and enhance susceptibility to cell death induction. As we speculated, the expression level of p-FAK and p-ERK1/2 gradually declined after MDA-MB-231 cells were treated with various formulations of NPs (Fig. 5(b)), accompanied by the increase of

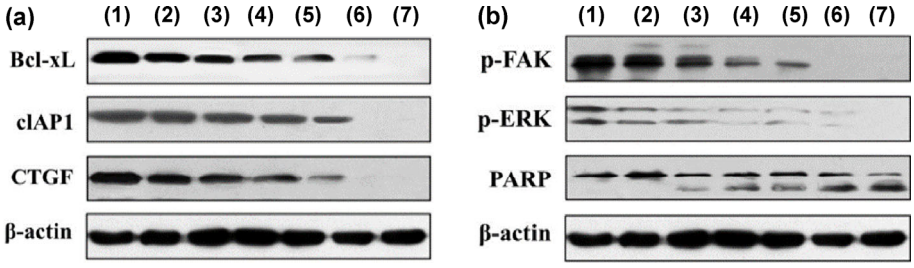

Figure 5 MDA-MB-231 cells were incubated with different formulations with 30 μg/mL Dox for 24 h to measure the protein levels by using WB. (a) Bcl-xL and clAP1 are functional effectors in CTGF-mediated drug resistance. Protein levels of Bcl-xL, clAP1, and CTGF were confirmed using a WB analysis. (b) Apoptosis related proteins, p-FAK, p-ERK, and PARP, were also examined using a WB analysis. (1) Control; (2) rmSiO$_2$ NPs; (3) Dox; (4) rmSiO$_2$@Dox NPs; (5) rmSiO$_2$@Dox@HA NPs; (6) rmSiO$_2$@siRNA@Dox NPs; and (7) rmSiO$_2$@siRNA@Dox@HA NPs.

poly ADP-ribose polymerase (PARP) cleavage, meaning MDA-MB-231 cells should have a more susceptible response to drug stimulation. With the measured level of protein expression, we were able to determine that the NPs that incorporated siRNA possessed excellent efficacy in reducing drug resistance in breast cancer cells.

3.5 Therapeutic evaluation of HACT NPs in breast cancer bearing mice

In the targeting cascade for the *in vivo* experiments, the PEGA-pVEC peptide offered a secondary targeting ligand for directing the drug vehicle to the tumor tissue. To evaluate the *in vivo* effect of the targeting HACT NPs, MDA-MB-231 cells were grafted into the right forelimb of female nude mice, which were treated with the NPs loaded with Dox and siRNA (3 mg/kg Dox, 16 mg/kg rmSiO$_2$) six times at three-day intervals. HA and peptide co-modified NPs loaded with siRNA (HACT NPs) exhibited the strongest effect on inhibiting tumor growth compared with other groups, such as saline, free Dox, and rmSiO$_2$@Dox@HA NPs (Figs. 6(a)–6(c)). A significant difference in the tumor growth inhibition occurred between rmSiO$_2$@Dox@HA NPs and rmSiO$_2$@siRNA@Dox@HA NPs, suggesting that the siRNA on the complex played an essential part in improving therapeutic efficacy. Moreover, HACT NPs showed a higher tumor growth-inhibiting effect than rmSiO$_2$@siRNA@Dox@HA NPs, indicating the secondary targeting ligand PEGA-pVEC peptide made a certain contribution to the accumulation and permeation of HACT NPs in the tumor. During the period of treatment, the body weight of the mice in these groups presented a similar increasing trend, confirming that the HACT NPs produced few adverse effects on the normal organs (Fig. S7 in the ESM). By weighing the tumor tissue under different treatment conditions, we found that the mice treated with HACT NPs presented a much higher tumor inhibition ratio (Fig. 6(d)), even doubling the therapeutic effect of the Dox group. The Dox concentrations in the blood were detected after intravenous injection of Dox and HACT NPs (Fig. 6(e)). Unlike the rapid clearance of free Dox in the body, the encapsulated Dox had a better sustained release effect, reflecting that the HA outer shell of HACT NPs increased the *in vivo* stability of Dox and rendered the long circulating behavior. The above results further highlight the importance of the secondary targeting ligand PEGA-pVEC peptide in recognizing the tumor region *in vivo*, boosting the therapeutic effect and the reliability of the HA shell for drug transportation in the circulation system.

The H&E stained tumor sections showed the maximum inhibition of tumor cell division and proliferation after the mice were treated with HACT NPs (Fig. 7(a)). In addition, treatment with HACT NPs presented the highest downregulation of Bcl-xL, cIAP1, and CTGF expression levels (Fig. 7(b)) and remarkably decreased the expression of the proteins related to cellular protection from apoptosis in the tumors (Fig. 7(c)). Meanwhile, to evaluate the side effects of different formulations, the main organs were harvested and stained with H&E, such as the

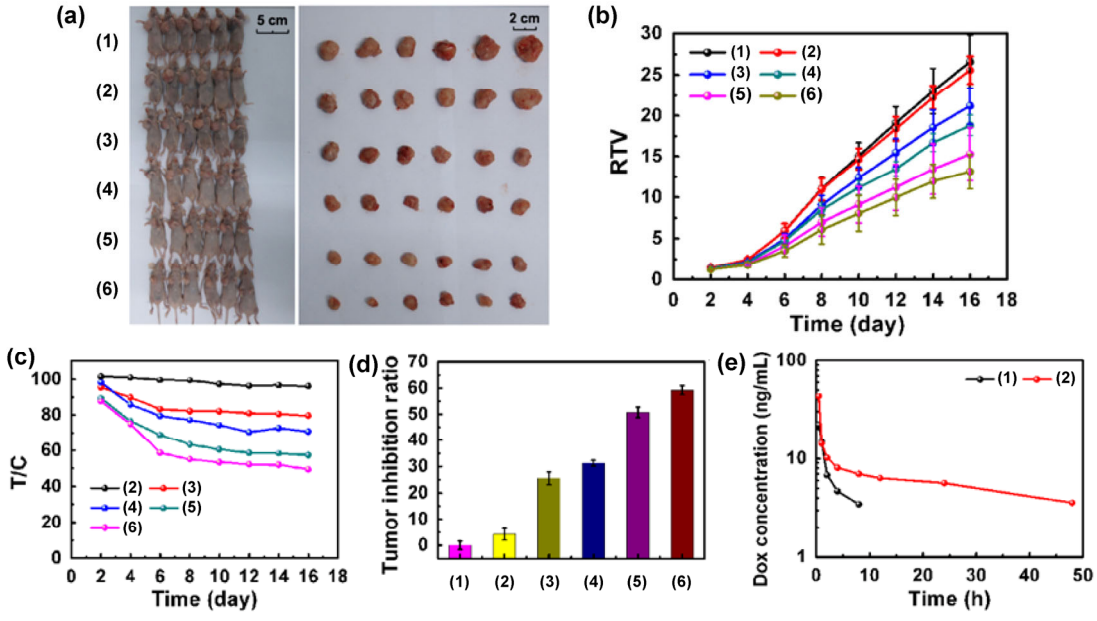

Figure 6 (a) The images of MDA-MB-231 tumor bearing mice and stripped tumors after treatment with different formulations with 3 mg/kg of Dox day 18. (b) Change of relative tumor volume (RTV) upon different treatments. Data are represented as the mean ± SD (n = 6). (c) Relative tumor proliferation rate (T/C (%) = TRTV/CRTV × 100, TRTV: RTV of treatment group; CRTV: RTV of model control group). (d) The tumor inhibition ratio of different formulations. (1) Control; (2) rmSiO$_2$ NPs group; (3) Dox group; (4) rmSiO$_2$@Dox@HA NPs group; (5) rmSiO$_2$@siRNA@Dox@HA NPs group; and (6) HACT NPs group. (e) Drug metabolism curve. (1) Dox and (2) HACT NPs.

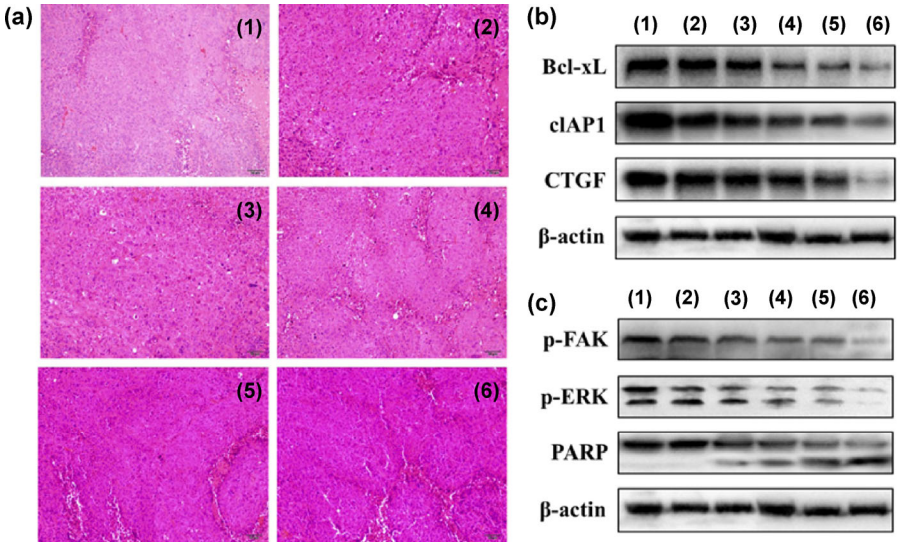

Figure 7 (a) Histological observation of the tumors of the mice after different treatments. The tumor sections were stained with H&E. The scale bar represents 20 μm. (b) and (c) Related protein expression in the tumor harvested from the mice after treatment was determined using a WB analysis. (1) Control; (2) rmSiO$_2$ NPs group; (3) Dox group; (4) rmSiO$_2$@Dox@HA NPs group; (5) rmSiO$_2$@siRNA@Dox@HA NPs group; and (6) HACT NPs group.

heart, liver, spleen, lung, kidney, and brain. The mice treated with HACT NPs displayed no pathological change compared to those treated with saline (Fig. S8 in the ESM), which was attributed to the low retention and low premature leakage of the nanocarriers in the normal organs. These histological observations and protein expression analyses suggest that the cascaded targeting nanocarriers embedded with siRNA were

capable of regulating the drug resistance of the tumor *in vivo* with little harm to normal tissues and organs.

4 Conclusions

We have successfully developed activatable HAase, siRNA-involved cascaded targeting NPs to overcome the drug resistance of CTGF-overexpressing breast cancer. The rmSiO$_2$-based HACT NPs were formulated with cascade targeting media from the PEGA-pVEC peptide and HA, and encapsulated with a combination of therapeutic agents of siRNA and Dox, manifesting better *in vivo* tumor-targeting and anti-cancer efficacy than single targeting ligand vectors and chemotherapy strategies. In virtue of the HA outer shell, the nanocarriers effectively protected siRNA and Dox against many obstacles from the point of administration to the delivery sites, and allowed activatable HAase drug release. We anticipate that the cascaded targeting nanocarriers will provide a versatile nanomedical platform for the highly precise transportation of multiple therapeutic agents in a synergistic treatment and strategy to overcome the drug resistance of specific cancers by silencing the related gene may potentially promote the clinical effect of wide-spectrum anti-cancer drugs.

Acknowledgements

This research was supported by National Natural Science Foundation of China (Nos. 21335004, 21475057, 21575061, and 21622505).

Electronic Supplementary Material: Supplementary material (particle size distribution of NPs, the adsorption amount of Dox on rmSiO$_2$ or rmSiO$_2$@PEI NPs, nitrogen adsorption–desorption and pore size distribution curve of rmSiO$_2$, the change profile of hydrodynamic diameter and zeta potential, real-time confocal fluorescence images, the inhibition ratio of rmSiO$_2$ NPs on MDA-MB-231 cells, the body weights of tumor-bearing mice and H&E stained images of tissue sections) is available in the online version of this article at http://dx.doi.org/10.1007/s12274-016-1328-y.

References

[1] Siegel, R.; Naishadham, D.; Jemal, A. Cancer statistics, 2012. *CA Cancer J. Clin.* **2012**, *62*, 10–29.

[2] Siegel, R.; DeSantis, C.; Virgo, K.; Stein, K.; Mariotto, A.; Smith, T.; Cooper, D.; Gansler, T.; Lerro, C.; Fedewa, S. et al. Cancer treatment and survivorship statistics, 2012. *CA Cancer J. Clin.* **2012**, *62*, 220–241.

[3] Bork, P. The modular architecture of a new family of growth regulators related to connective tissue growth factor. *FEBS Lett.* **1993**, *327*, 125–130.

[4] Lau, L. F.; Lam, S. C. T. The CCN family of angiogenic regulators: The integrin connection. *Exp. Cell Res.* **1999**, *248*, 44–57.

[5] Kondo, S.; Kubota, S.; Shimo, T.; Nishida, T.; Yosimichi, G.; Eguchi, T.; Sugahara, T.; Takigawa, M. Connective tissue growth factor increased by hypoxia may initiate angiogenesis in collaboration with matrix metalloproteinases. *Carcinogenesis* **2002**, *23*, 769–776.

[6] Xie, D.; Nakachi, K.; Wang, H.; Elashoff, R.; Koeffler, H. P. Elevated levels of connective tissue growth factor, WISP-1, and CYR61 in primary breast cancers associated with more advanced features. *Cancer Res.* **2001**, *61*, 8917–8923.

[7] Chen, P. S.; Wang, M. Y.; Wu, S. N.; Su, J. L.; Hong, C. C.; Chuang, S. E.; Chen, M. W.; Hua, K. T.; Wu, Y. L.; Cha, S. T. et al. CTGF enhances the motility of breast cancer cells via an integrin-αvβ3-ERK1/2-dependent S100A4-upregulated pathway. *J. Cell Sci.* **2007**, *120*, 2053–2065.

[8] Mehlen, P.; Puisieux, A. Metastasis: A question of life or death. *Nat. Rev. Cancer* **2006**, *6*, 449–458.

[9] Wang, M. Y.; Chen, P. S.; Prakash, E.; Hsu, H. C.; Huang, H. Y.; Lin, M. T.; Chang, K. J.; Kuo, M. L. Connective tissue growth factor confers drug resistance in breast cancer through concomitant up-regulation of Bcl-xL and cIAP1. *Cancer Res.* **2009**, *69*, 3482–3491.

[10] Salcher, E. E.; Wagner, E. Chemically programmed polymers for targeted DNA and siRNA transfection. In *Nucleic Acid Transfection*;Bielke, W.; Erbacher, C., Eds.; Springer: Berlin, Heidelberg, Germany, 2010; pp 227–249.

[11] Pecot, C. V.; Calin, G. A.; Coleman, R. L.; Lopez-Berestein, G.; Sood, A. K. RNA interference in the clinic: Challenges and future directions. *Nat. Rev. Cancer* **2011**, *11*, 59–67.

[12] Thompson, J. D. Clinical development of synthetic siRNA therapeutics. *Drug Discov. Today Ther. Strateg.* **2013**, *10*, e133–e138.

[13] Peer, D.; Karp, J. M.; Hong, S.; Farokhzad, O. C.; Margalit, R.; Langer, R. Nanocarriers as an emerging platform for cancer therapy. *Nat. Nanotechnol.* **2007**, *2*, 751–760.

[14] Jain, R. K.; Stylianopoulos, T. Delivering nanomedicine to solid tumors. *Nat. Rev. Clin. Oncol.* **2010**, *7*, 653–664.

[15] Cabral, H.; Nishiyama, N.; Kataoka, K. Supramolecular nanodevices: From design validation to theranostic nanomedicine. *Acc. Chem. Res.* **2011**, *44*, 999–1008.

[16] Mo, R.; Jiang, T. Y.; DiSanto, R.; Tai, W. Y.; Gu, Z. ATP-triggered anticancer drug delivery. *Nat. Commun.* **2014**, *5*, 3364.

[17] Zhang, Q.; Ge, J. P.; Goebl, J.; Hu, Y. X.; Lu, Z. D.; Yin, Y. D. Rattle-type silica colloidal particles prepared by a surface-protected etching process. *Nano Res.* **2009**, *2*, 583–591.

[18] Li, L. L.; Tang, F. Q.; Liu, H. Y.; Liu, T. L.; Hao, N. J.; Chen, D.; Teng, X.; He, J. Q. *In vivo* delivery of silica nanorattle encapsulated docetaxel for liver cancer therapy with low toxicity and high efficacy. *ACS Nano* **2010**, *4*, 6874–6882.

[19] Yuan, F.; Leunig, M.; Huang, S. K.; Berk, D. A.; Papahadjopoulos, D.; Jain, R. K. Microvascular permeability and interstitial penetration of sterically stabilized (stealth) liposomes in a human tumor xenograft. *Cancer Res.* **1994**, *54*, 3352–3356.

[20] Campbell, R. B.; Fukumura, D.; Brown, E. B.; Mazzola, L. M.; Izumi, Y.; Jain, R.; Torchilin, K. V. P.; Munn, L. L. Cationic charge determines the distribution of liposomes between the vascular and extravascular compartments of tumors. *Cancer Res.* **2002**, *62*, 6831–6836.

[21] Heldin, C. H.; Rubin, K.; Pietras, K.; Östman, A. High interstitial fluid pressure-an obstacle in cancer therapy. *Nat. Rev. Cancer* **2004**, *4*, 806–813.

[22] Burrows, F. J.; Thorpe, P. E. Vascular targeting—A new approach to the therapy of solid tumors. *Pharmacol. Ther.* **1994**, *64*, 155–174.

[23] Hashizume, H.; Baluk, P.; Morikawa, S.; McLean, J. W.; Thurston, G.; Roberge, S.; Jain, R. K.; McDonald, D. M. Openings between defective endothelial cells explain tumor vessel leakiness. *Am. J. Pathol.* **2000**, *156*, 1363–1380.

[24] Leu, A. J.; Berk, D. A.; Lymboussaki, A.; Alitalo, K.; Jain, R. K. Absence of functional lymphatics within a murine sarcoma: A molecular and functional evaluation. *Cancer Res*. **2000**, *60*, 4324–4327.

[25] Ding, J.; Yao, J.; Xue, J. J.; Li, R.; Bao, B.; Jiang, L. P.; Zhu, J. J.; He, Z. W. Tumor-homing cell-penetrating peptide linked to colloidal mesoporous silica encapsulated (–)-epigallocatechin-3-gallate as drug delivery system for breast cancer therapy *in vivo*. *ACS Appl. Mater. Interfaces* **2015**, *7*, 18145–18155.

[26] Li, K.; Liu, H.; Gao, W.; Chen, M.; Zeng, Y.; Liu, J. J.; Xu, L.; Wu, D. C. Mulberry-like dual-drug complicated nanocarriers assembled with apogossypolone amphiphilic starch micelles and doxorubicin hyaluronic acid nanoparticles for tumor combination and targeted therapy. *Biomaterials* **2015**, *39*, 131–144.

[27] Myrberg, H.; Zhang, L. L.; Mäe, M.; Langel, Ü. Design of a tumor-homing cell-penetrating peptide. *Bioconjugate Chem.* **2008**, *19*, 70–75.

[28] Essler, M.; Ruoslahti, E. Molecular specialization of breast vasculature: A breast-homing phage-displayed peptide binds to aminopeptidase P in breast vasculature. *Proc. Natl. Acad. Sci. USA* **2002**, *99*, 2252–2257.

[29] Elmquist, A.; Lindgren, M.; Bartfai, T.; Langel, Ü. VE-cadherin-derived cell-penetrating peptide, *p*VEC, with carrier functions. *Exp. Cell. Res.* **2001**, *269*, 237–244.

[30] Jiang, T. Y.; Mo, R.; Bellotti, A.; Zhou, J. P.; Gu, Z. Gel-liposome-mediated co-delivery of anticancer membrane-associated proteins and small-molecule drugs for enhanced therapeutic efficacy. *Adv. Funct. Mater.* **2014**, *24*, 2295–2304.

[31] Wang, Z. Z.; Chen, Z. W.; Liu, Z.; Shi, P.; Dong, K.; Ju, E. G.; Ren, J. S.; Qu, X. G. A multi-stimuli responsive gold nanocage-hyaluronic platform for targeted photothermal and chemotherapy. *Biomaterials* **2014**, *35*, 9678–9688.

[32] Zhang, F.; Wan, Y.; Yu, T.; Zhang, F. G.; Shi, Y. F.; Xie, S. H.; Li, Y. G.; Xu, L.; Tu, B.; Zhao, D. Y. Uniform nanostructured arrays of sodium rare-earth fluorides for highly efficient multicolor upconversion luminescence. *Angew Chem., Int. Ed.* **2007**, *46*, 7976–7979.

[33] Bhang, S. H.; Won, N.; Lee, T. J.; Jin, H.; Nam, J.; Park, J.; Chung, H.; Park, H. S.; Sung, Y. E.; Hahn, S. K. et al. Hyaluronic acid-quantum dot conjugates for *in vivo* lymphatic vessel imaging. *ACS Nano* **2009**, *3*, 1389–1398.

[34] Li, J.; Huo, M. R.; Wang, J.; Zhou, J. P.; Mohammad, J. M.; Zhang, Y. L.; Zhu, Q. N.; Waddad, A. Y.; Zhang, Q. Redox-sensitive micelles self-assembled from amphiphilic hyaluronic acid-deoxycholic acid conjugates for targeted intracellular delivery of paclitaxel. *Biomaterials* **2012**, *33*, 2310–2320.

[35] Huber, W.; Koella, J. C. A comparison of three methods of estimating EC_{50} in studies of drug resistance of malaria parasites. *Acta Trop.* **1993**, *55*, 257–261.

[36] Isacke, C. M.; Yarwood, H. The hyaluronan receptor, CD44. *Int. J. Biochem. Cell Biol*. **2002**, *34*, 718–721.